Room-temperature logic-in-memory operations in single-metallofullerene devices

Jing Li,[1,4] Songjun Hou,[2,4] Yang-Rong Yao,[1,4] Chengyang Zhang,[1,4] Qingqing Wu,[2] Hai-Chuan Wang,[1] Hewei Zhang,[1] Xinyuan Liu,[1] Chun Tang,[1] Mengxi Wei,[1] Wei Xu,[1] Yaping Wang,[1] Jueting Zheng,[1] Zhichao Pan,[1] Lixing Kang,[3] Junyang Liu,[1] Jia Shi,[1] Yang Yang,[1] Colin J. Lambert,[2*] Su-Yuan Xie,[1*] Wenjing Hong[1*]

[1] State Key Laboratory of Physical Chemistry of Solid Surfaces, College of Chemistry and Chemical Engineering & IKKEM, Xiamen University, Xiamen, 361005, P. R. China.
[2] Department of Physics, Lancaster University, Lancaster LA 14 YB, United Kingdom
[3] Key Laboratory of Multifunctional Nanomaterials and Smart Systems, Division of Advanced Materials, Suzhou Institute of Nano-Tech and Nano-Bionics, Chinese Academy of Sciences, Suzhou 215123, China
[4] These authors contributed equally: Jing Li, Songjun Hou, Yang-Rong Yao, Chengyang Zhang
*e-mail: c.lambert@lancaster.ac.uk, syxie@xmu.edu.cn, and whong@xmu.edu.cn

Abstract

In-memory computing provides an opportunity to meet the growing demands of emerging massive data-driven applications such as machine learning,[1] by co-locating logic operations and data storage.[2,3] Despite being regarded as the ultimate solution for high-density integration and low-power manipulation, the critical step of operating a spin or an electric dipole at the single-molecule scale[4,5] to realize in-memory logic functions has yet to be realized at room temperature. This is because the spin is subject to random thermal switching and the electric dipole has not been studied at room temperature.[6,7] Here, we report an experimental demonstration of logic-in-memory operations, based on single electric dipole flipping in a two-terminal single-metallofullerene ($Sc_2C_2@C_s$(hept)-C_{88}) device at room temperature. By applying a low voltage of ±0.8 V to the single-metallofullerene junction, we found that the digital information recorded among the different dipolar states could be reversibly encoded *in-situ* and stored. Consequently, we demonstrated fourteen types of Boolean logic operations in the single-metallofullerene device. Furthermore, density functional theory (DFT)

calculations reveal that the microscopic physical mechanism of non-volatile memory behavior comes from the electrical-field-driven dipole reorientation of the [Sc$_2$C$_2$] group in the fullerene cage. Our findings show that single permanent electrical dipoles can be employed to develop the smallest room-temperature storage devices. This proof of concept represents a significant step towards room-temperature electrically manipulated, low-power, two-terminal in-memory logic devices at the sub-nanometer level, and it identifies a new direction for in-memory computing using nanoelectronic devices.

<mark>Introduction</mark>

Logic-in-memory devices are the fundamental units of in-memory and neuromorphic computing.[8-10] Their logic-in-memory operations have been demonstrated in non-volatile memory devices,[9,11] such as resistive switching random access memory (RRAM),[12] phase-change memory (PCM),[13] magnetoresistive random access memory (MRAM),[14] and ferroelectric random access memory (FeRAM).[15,16] For further miniaturization of electronic devices and optimization of their power efficiency, molecular-scale non-volatile memory devices,[17-19] such as self-assembled monolayer or molecular thin films,[20-24] have been demonstrated to operate at a low operating voltage below 1.0 V. This implies that single-molecule non-volatile memory devices[5,25,26] may provide the ultimate solution for the realization of logic-in-memory computing. However, due to experimental challenges in the fabrication of single-molecule devices and the control of different molecular states at room temperature, the logic-in-memory operations in single-molecule devices have yet to be explored. Ideally, compared to macroscopic or mesoscopic devices, manipulating the spin or electric dipole is a better solution for the realization of in-memory logic operations at the single-molecule

52 scale.[4,5] Low-temperature single electrical dipole bistability has recently been demonstrated in a

53 gate-controlled Gd@C_{82}-based three-terminal device at temperatures below 1.6 K,[5] but room-

54 temperature single electrical dipole bistability remains elusive in experiments.

55

56 Several challenges for the logic-in-memory operation in an all-electrically driven single-molecule

57 device at room temperature remain to be addressed. First, at a temperature T, bistable states ('0' and

58 '1') of the target molecule must be separated by an energy barrier $U > k_BT$ (**Fig. 1b**) to prevent

59 spontaneous and random switching between different stable states.[5,7,27-30] In addition, these states

60 should provide different charge transport channels, resulting in distinguishable electrical read-out

61 signals.[5] More importantly, the energy barrier should be tunable with an external electric field,

62 enabling reversible switching of the bistable states.[25,31] Regarding spin at the single-molecule scale,

63 a single-molecule magnet (SMM)[29,30] is promising as one of the smallest storage devices with

64 sufficient environmental tolerance. However, the energy barrier that prevents random spin switching

65 is too small (typically $< \approx 10$ meV), which restricts the operating temperature to the liquid helium

66 temperatures rather than room temperature.[32] Compared to SMMs, single independent permanent

67 dipoles free of inter-dipole coupling can be stabilized at room temperature by anisotropic energy of

68 several hundred meV,[28] suggesting that polarization can be stabilized and manipulated at room

69 temperature. When an external electric field is applied to a polarized permanent dipole, the energy

70 levels of the states are shifted in opposite directions, as shown in Fig. 1c, and thus, the molecule

71 will be stabilized in the lowest-energy state, which switches when the external electric field reaches

72 a threshold value.[5] In order to achieve room-temperature operation, the energy barrier should be

73 high enough to prevent the spontaneous switching induced by thermal fluctuations and local

74   heating,[33] (ie $U > k_B T$, where T is ~300 K and therefore $k_B T \sim 25$ meV)   (**Fig. 1b**), but it must not

75   be too high to avoid an increase of energy consumption and potential damage to the molecular

76   device.
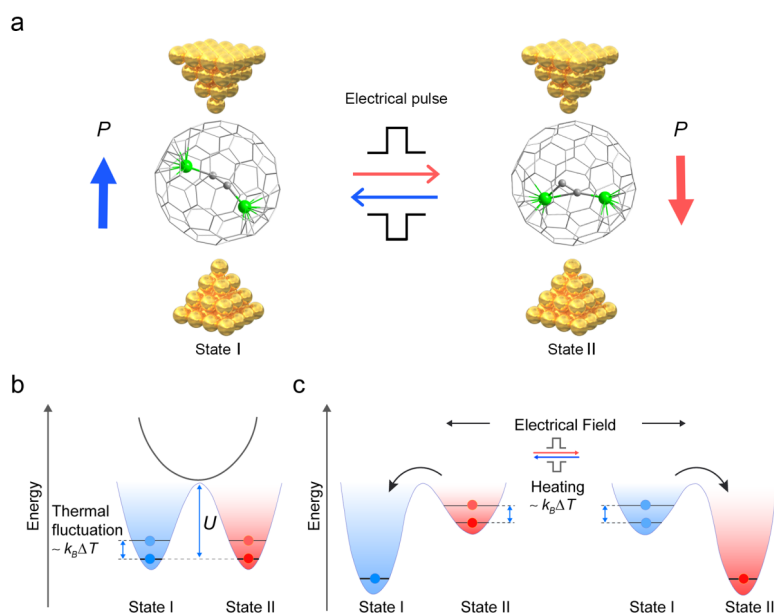
77

78   **Fig. 1| The mechanism of the single-metallofullerene memory device. a,** Optimized single $Sc_2C_2@C_s$(hept)-C_{88}

79   junction configurations when State I and State II are embedded in two-terminal gold electrodes. *P* represents the

80   polarized permanent dipole direction of the molecule. The two states I and II can switch reversibly through the

81   external electric field. **b,** Energy level diagram of bistability without external electric fields. The States I and II are

82   separated by an energy barrier *U*. The vibration excitation comes from the thermal fluctuation $\sim k_B \Delta T$ in the

83   environment, which is lower than the energy barrier. **c,** Energy level diagram of bistability under electric fields. The

84   energy levels shift in opposite directions due to coupling between the opposite polarized permanent dipole and the

85   electric field. During operation, joule heat ($\sim k_B \Delta T$) exists.

86

87   Here we demonstrate the room-temperature non-volatile memory behavior and logic-in-memory

88   operations of two-terminal single endohedral metallofullerene $Sc_2C_2@C_s$(hept)-C_{88} devices using

89   the scanning tunneling microscope break junction (STM-BJ) technique (**Fig. 1a**). Our *in-situ*

90   experiments demonstrate that these conductance switches can serve as non-volatile memory with a

91   pulsed voltage of ±0.8 V, and that logic-in-memory operations of fourteen Boolean functions can be

92   realized in these devices. DFT calculations reveal that this switching stems from the electrical-field-

93   driven reorientation of the dipole of the [Sc_2C_2] group in the fullerene cage.

94

95   **Results and discussion**

96   As a prototypical molecule to demonstrate the room-temperature single electrical dipole bistability,

97   endohedral metallofullerene molecules were chosen,[34,35] because of their tunable single permanent

98   dipoles located in the fullerene cages,[5,7,36] which are potential candidates to show single electrical

99   dipole bistability.[7,36] Recent theoretical calculations by Jaroš et al.[7] showed that the encapsulation

100   energy and chemical bonding energy between a Sc^{3+} ion and the fullerene cage are suitable for

101   room-temperature switching. Here we examine the potential of $Sc_2C_2@C_s$(hept)-C_{88} to provide

102   distinguishable electrical read-out signals, because it has good stability at room temperature and low

103   symmetry due to the presence of a special heptagonal ring. The encapsulated [Sc_2C_2] group is

104   disordered in the cage according to the crystal structure, indicating that there are several stable states

105   with similar ground energy minima (**Fig. 1b**).[37] Furthermore, the [Sc_2C_2] group has a quasi-

106   permanent dipole, making it possible to rotate within the cage when an electric field ($\sim 10^8$ V m^{-1},

107   **Fig. 1c**) is applied.[7,37-39] Therefore, when applying a strong electric field to the sub-nanometer

108   metallofullerene junction, the coupling between the quasi-permanent dipole of the [Sc_2C_2] group

109   and oriented strong electric field in the nanogap may trigger the rotation of the [Sc_2C_2] group at

110   room temperature.

111   Single-$Sc_2C_2@C_s$(hept)-C_{88} junctions were fabricated, and their conductance was measured by

112   repeatedly forming and breaking gold point contacts using the STM-BJ technique[40,41] in the

113   corresponding solution at room temperature. During the retraction of the gold tip, conductance

114   plateaus between 10^{-2} and 10^{-3} G_0 (where $G_0 = 2e^2/h = 77.6$ μS) appeared (**Fig. 2a inset**), indicating

115   the formation of Au-metallofullerene-Au junctions. Thousands of conductance traces were collected

116   to construct 1D conductance histograms (**Fig. 2a**) and 2D conductance-displacement histograms

117   (**Fig. 2b**). The most possible conductance value of single-metallofullerene junctions was determined

118   to be $10^{-2.5}$ G_0 (0.25 μS), which corresponds to the position of the conductance intensity cloud in the

119   2D conductance-displacement histogram (**Fig. 2b**). We found the displacement distribution to be

120   located at ~0.65 nm as fitted by a Gaussian function (**Fig. 2b inset**), indicating that the gold-gold

121   distance was approximately 1.15 nm after calibration with a 0.5 nm snap-back distance.[42] This

122   distance was consistent with the sum of the cage length (~0.8 nm from the crystal structure) and the

123   double length of the Au-π bond (~0.2 nm), suggesting the formation of single-metallofullerene

124   junctions.[43,44]
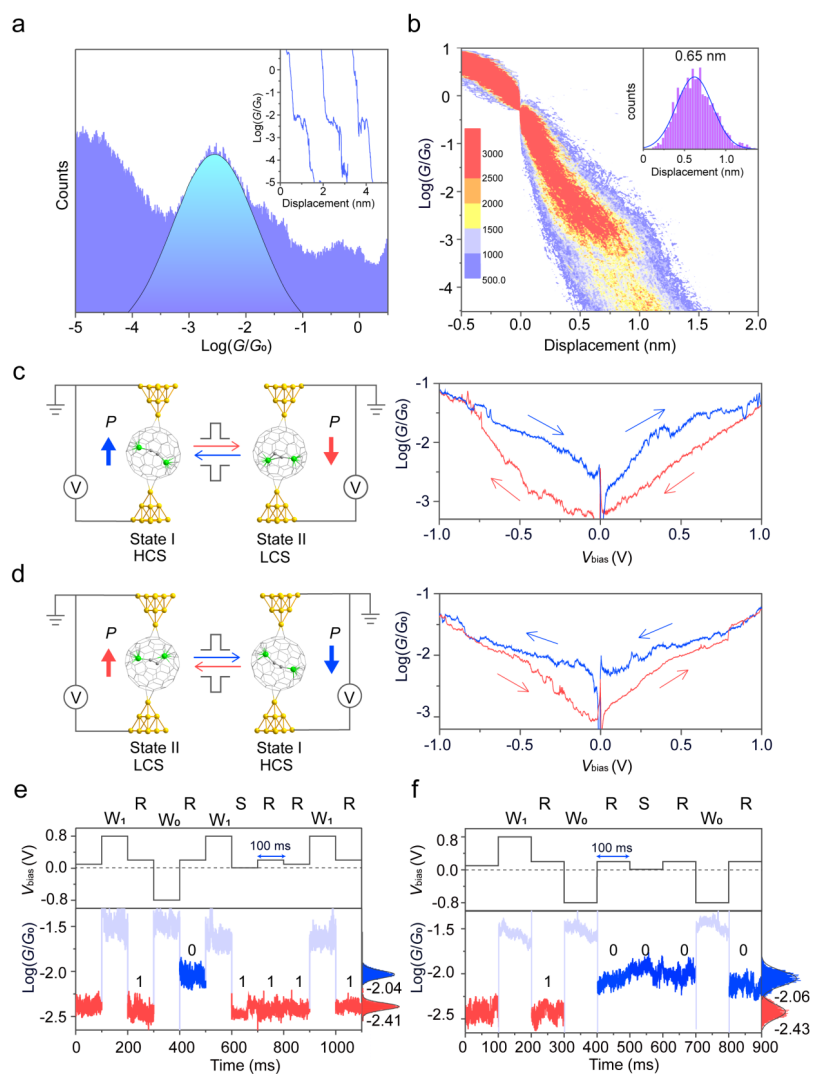
Fig. 2| Single-molecule conductance measurements and the *in-situ* two-conductance-state switching and storage operations of single-$Sc_2C_2@C_s$(hept)-C_{88} devices. a-b, Logarithm-binned 1D histogram and 2D conductance–displacement histogram constructed from the single-molecule conductance measurements of $Sc_2C_2@C_s$(hept)-C_{88} under +0.1 V, respectively. **c-d,** The two typical types of Au-molecule-Au junctions according to the theoretically calculated dipole direction and electrode arrangements, and their related single *G-V* curves. LCS and HCS indicate low- and high-conductance states, respectively. **e-f,** The non-volatile memory behavior of the device. The top figure presents the bias voltage plotted versus time. Since the statistical threshold voltages were ~±0.7 V, we chose +0.8 V (marked as W_1) to write the '1' state, -0.8 V (marked as W_0) to write the '0' state, and

134 +0.2 V (marked as R) to read out the digital information through the conductance of the molecule. To ensure data

135 collection, we treated +0.01 V as zero voltage (marked as S) to exhibit the non-volatile memory characteristics

136 during the measurements. The bottom figure shows the conductance plotted against the same time as the bias voltage.

137 The 'read' high- and low-conductance states are highlighted in blue and red, respectively.

138

139 To investigate the switching behavior of a single-metallofullerene junction, the conductance versus

140 bias voltage (G-V) curve was measured by sweeping the bias voltage while holding the

141 metallofullerene between the two electrodes, leading to conductance in the range from 10^{-2} to 10^{-3}

142 G_0 (see the Methods section for details).[45] More than 1,000 G-V curves were collected with a cyclic

143 sequence from 0 V → 1 V→ 0 V → -1 V→ 0 V. Approximately 81% (941 out of 1162 curves) of

144 the single G-V curves showed hysteresis loops (Supplementary **Fig. 1**) and the loops could be

145 divided into two types: the forward (blue) curve was above the backward (red) curve (right column

146 of **Fig. 2c**) or the opposite (right column of **Fig. 2d**). The two types of G-V curves were attributed

147 to two geometries of the single-molecule junctions with a polarized permanent dipole, including

148 those with a polarized dipole pointing towards the tip and those pointing away from the tip (left

149 column of **Figs. 2c-2d**). Curves from different sweep directions were analyzed and two average G-

150 V curves were obtained from the two-dimensional G-V histogram shown in Supplementary **Figs.**

151 **3a-3b**. The open loops in the two G-V curves indicated that the junctions retained an internal

152 conductance state based on the history of the external voltage and current, similar to bipolar

153 conductance switches (BCSs).[8,12] From the statistical G–V curves, the open-loop was closed at a

154 bias voltage of ~±0.7 V, showing a low statistical threshold bias voltage (Supplementary **Figs. 3a-**

155 **3b**). A low threshold bias voltage was also observed in other endohedral metallofullerene molecules

156 measured at low temperatures by scanning tunneling microscopy (STM).[46,47] To reveal the source

157 of the hysteresis loop, G-V plots of $Sc_2C_2@C_s$(hept)-C_{88} in a nitrogen protected glove box, C_{70} and

158   OPE (1,2-bis(4-(methylthio)phenyl)ethyne) without moveable dipoles were measured as control

159   experiments with the identical experimental sequence (Supplementary **Figs. 3c-3d and 4**). When

160   measured in the glove box, the same hysteresis loop was observed in $Sc_2C_2@C_s$(hept)-C_{88}, ruling

161   out the possibility that polar molecules, such as water, adsorbed on the surface of the fullerene cages

162   induce the hysteresis (Supplementary **Fig. 4**). No hysteresis loop was observed in the *G-V* plots of

163   C_{70} and OPE (Supplementary **Figs. 3c-3d**), suggesting that the inner dipole in the cavity of

164   fullerenes indeed plays a crucial role in the electrical hysteresis.

165   The open hysteresis loops observed in the *G-V* curves offered the potential of non-volatile memory

166   operation, but first the storage of information at zero electric fields must be demonstrated. To further

167   characterize the non-volatile memory behavior of our devices, we undertook *in-situ* "two-

168   conductance-state switching" and "storage" operations by applying pulsed bias voltage sequences

169   to the single-fullerene junctions, as shown in **Figs. 2e-2f** and Supplementary **Fig. 5**. After the bias

170   voltage operation, a high-conductance state (HCS, blue) and low-conductance state (LCS, red)

171   yielded the distinguishable switching ratios ($R = \frac{c_{HCS}}{c_{LCS}} \times 100\%$) ranging from ~150% to ~500%.

172   More importantly, the conductance states stored after the period of zero bias voltage (marked as S

173   in **Figs. 2e-2f**) were retained, demonstrating that the output conductance state was non-volatile and

174   remained stored without bias. We also evaluated the switching ratio versus time and found that it

175   remained almost constant over four hours in different junctions in one experiment (Supplementary

176   **Fig. 7**) and also after 19 reversible switching cycles in single-molecule junction (Supplementary

177   **Fig. 8**), suggesting that no degradation occurs under the electric field due to the excellent chemical

178   stability of the molecules. We have also evaluated the switching time of the junctions that it was

179   less than 0.15 ms (Supplementary **Fig. 9** and Supplementary Information S4), which is much faster

180 ==than the== switching time ==of the spin-crossover based single-molecule memristance[48] and sufficiently==

181 ==fast for the potential device applications.== The homologues of $Sc_2C_2@D_{2d}(23)$-C_{84} and

182 $Sc_2C_2@C_{2v}(9)$-C_{86} also exhibited non-volatile memory characteristics (Supplementary **Fig. ==11==**),

183 indicating that endohedral metallofullerenes are promising candidates for binary memory devices

184 due to the presence of the inner dipole.
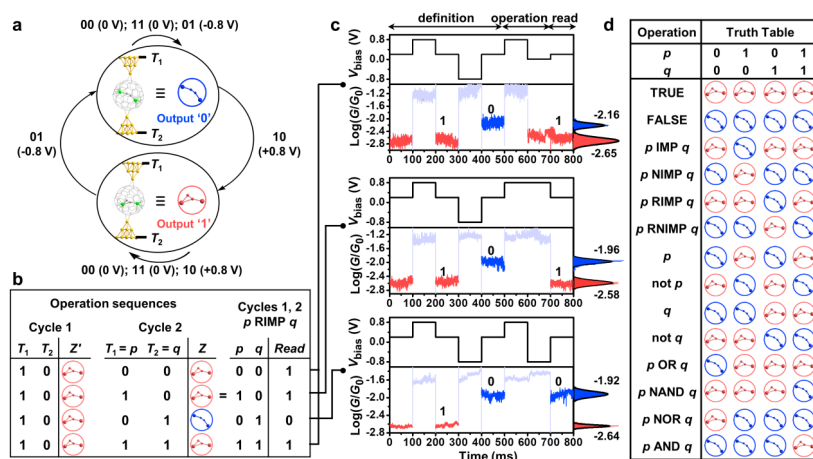
Fig. 3| Boolean logic operations in single-metallofullerene devices of $Sc_2C_2@C_s$(hept)-C_{88}. a, Logic operations of the single-metallofullerene device. The source and drain electrodes of the device are marked with T_1 and T_2. The bias voltage across the device is $0.8 \times (T_1$-$T_2)$ V, where T_1 and T_2 represent logic operations T_1T_2 including **00** (0 V), **01** (-0.8 V), **10** (+0.8 V), and **11** (0 V). Here **0** represents low potential, and **1** represents high potential. The low-conductance state (LCS) corresponds to the output logic value '1'. **b,** The truth tables show the operation sequence to the implication function "*p* RIMP *q*". **c,** Experimental demonstration of the "*p* RIMP *q*" logic operation. **d,** The truth table of fourteen fundamental Boolean logic functions for material implication obtained from our experiments.

194 Having demonstrated that the single-metallofullerene BCS devices could be considered as logic

195 gates, with switching voltages of ±0.8 V and that the output of the logic operation is stored as the

196 conductance of the metallofullerene with different states, as shown in Fig. 3a, we now proceed

197 towards the truth table for material implication. Logic terms such as logic variables *p* and *q*,

198 terminal T_1 and T_2, and logic values '0' and '1' were introduced into the system, as shown in **Fig.**

199   **3** and Supplementary **Table 1**. The logic variables p and q assume **0** or **1**, corresponding to voltage

200   levels applied to the junction terminals T_1 and T_2, where **0** represents the low potential (0 V) and **1**

201   represents the high potential (0.8 V). Consequently, the voltage levels applied to terminals T_1 and

202   T_2 are denoted as $0.8 \times T_1$ and $-0.8 \times T_2$, respectively, so that the bias voltage across the device is 0.8

203   $\times (T_1 - T_2)$. According to Fig. 3a, the reverse implication (RIMP) for an initial state $Z' =$ '1', and the

204   inverse implication (NIMP) for an initial state $Z' =$ '0' can be realized.

205   To verify the logic functions of RIMP and NIMP in our system, we designed pulse bias voltage

206   sequences to conduct the logic-in-memory operations.[8] Here, the state after an operation of $T_1 =$ **1**

207   and $T_2 =$ **0** (+0.8 V) is assigned a logical value '1' and the state after an operation of $T_1 =$ **0** and T_2

208   $=$ **1** (-0.8 V) is assigned a logical value '0' to discuss the logic operations. Since the conductance of

209   state '0' could be higher or lower than that of state '1' (**Figs. 2c-2d**), an initial characterization cycle

210   is performed before the logic operations to define the conductance values of states '0' and '1', as

211   shown in the "definition" regime in **Fig. 3c**. Subsequently, pulse bias sequences are applied in the

212   "operation" regime to execute the logic operation, followed by a "read" voltage (0.2 V) to read out

213   the logic value. Given that the logic operation of $T_1 =$ **1** and $T_2 =$ **1** is the same as that of $T_1 =$ **0** and

214   $T_2 =$ **0**, we demonstrate both logic functions in the single $Sc_2C_2@C_s$(hept)-C_{88} device, with six pulse

215   bias voltage sequences (**Fig. 3c** and Supplementary **Fig. 15b**). The low conductance state (LCS)

216   corresponding to state '1' is shown in **Fig. 3**, and the high conductance state (HCS) corresponding

217   to state '1' is shown in Supplementary **Fig. 16**. Clearly, if the initial output value is '1' or '0', the

218   output of the logic operation is always '1' or '0', except when $T_1 =$ **0** and $T_2 =$ **1** or $T_1 =$ **1** and $T_2 =$

219   **0**. Thus, we extracted the logic table of RIMP and NIMP (**Fig. 3b** and Supplementary **Fig. 15b**)

220   from the experiments, and found it to be consistent with the truth table of Boolean functions.

221   Therefore, the actual state Z after an operation can be defined by

222                         $Z = (T_1 \text{ RIMP } T_2) \cdot Z' + (T_1 \text{ NIMP } T_2) \cdot (\text{not } Z')$ (1)

223   where Z' represents the initial state. Either the TRUE ($T_1 = 1$, $T_2 = 0$) or FALSE ($T_1 = 0$, $T_2 = 1$) logic

224   operation can be realized to initialize the state to '1' or '0' (Supplementary **Fig. 15a**). Based on

225   equation (1), ten more material implication operations, including IMP, NOT, AND, etc., can be

226   implemented in a two- or three-cycle process by sequential application of p and q (Supplementary

227   **Table 1**). From the experimental results with the LCS corresponding to the state '1' and HCS

228   corresponding to state '0' (Supplementary **Fig. 15**), we summarized a material implication truth

229   table, as shown in **Fig. 3c** and Supplementary **Table 1**, which agreed with the Boolean function,

230   indicating that logic-in-memory operations were achieved in the single-metallofullerene devices

231   presented in this work. The fourteen basic material implication logic functions were experimentally

232   implemented in the single-$Sc_2C_2@C_s$(hept)-C_{88} devices, demonstrating the potential of

233   metallofullerene in the logic-in-memory devices.

234
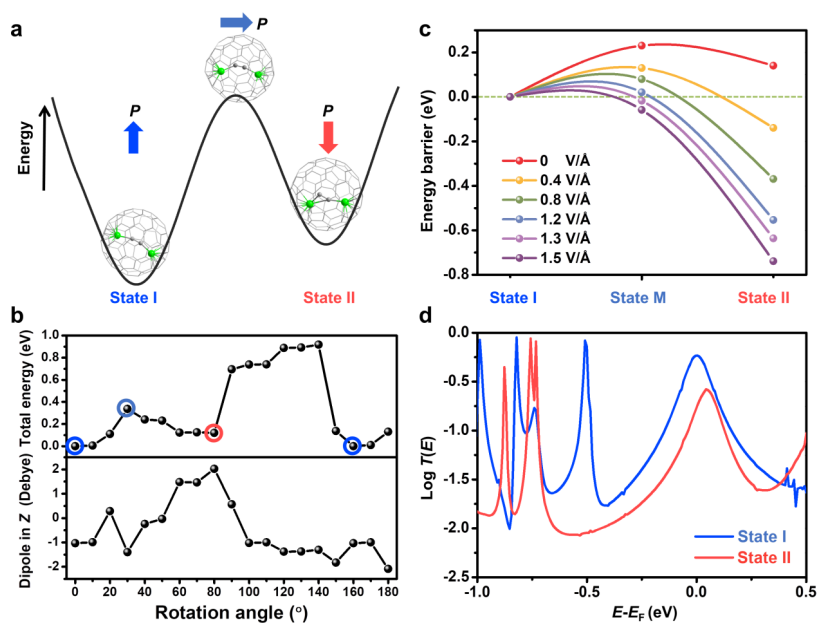
Fig. 4| The two-state memristive mechanism of $Sc_2C_2@C_s(hept)-C_{88}$. a, The geometries and energy profile corresponding to the two States I and II, and the intermediate State M. **b,** The fully relaxed energy landscape and the dipole moment in the *z*-direction when rotating the $[Sc_2C_2]$ cluster from 0 to 180° about an axis perpendicular to the long axis of the Sc_2C_2 molecule. **c,** The energy profile for these three states under different electric fields generated by a bias voltage. **d,** The transport function versus electron energy for State I and State II.

To investigate the mechanism of the non-volatile memory, theoretical calculations were carried out, starting with the published geometry[29,30] of $Sc_2C_2@C_s(hept)-C_{88}$ and fully relaxing the molecule using the DFT code SIESTA.[49-51] The resulting scandium carbide $[Sc_2C_2]$ cluster has a planar, zigzag structure. First, the energy profile associated with the rotation of the scandium carbide $[Sc_2C_2]$ cluster inside the C_{88} cage was investigated (Supplementary **Fig. 18a**). The most stable orientation of the cluster inside the cage agreed well with the published data.[37] As shown in Supplementary Fig. 18a, the energy barrier to rotate from 0º to 70º is about 0.227 eV. To further characterize the transition state, fcalculations were preformed within the Vienna Ab initio Simulation Package

250 <mark>(VASP 5.4.4)[52,53] using the climbing-image nudged elastic band (CI-NEB) method[54,55]. This yielded</mark>

251 <mark>a slightly higher energy barrier of 0.231 eV (Supplementary Fig. 18b-18e). The effect of interactions</mark>

252 <mark>with neighbouring fullerenes was also investigated and found to slightly reduce the energy barrier</mark>

253 <mark>(by < 0.05 eV), thereby facilitating the transformation of between the two states in C_{88} cage</mark>

254 <mark>(Supplementary **Fig. 19**).</mark> The influence of the gold tip on the orientation of the cluster inside the

255 cage was then examined by rotating the cage with the cluster together around the shorter axis of the

256 C_{88} cage (Supplementary **Fig. 20**). After relaxation, the cluster prefers to align more symmetrically

257 such that Sc and C are symmetrical relative to the mirror plane. From the energy profile

258 (Supplementary **Fig. 20**), three most stable structures were further adopted to study their energies

259 when the cluster is rotated within the cage (**Fig. 4**, Supplementary **Figs. 22-23**). The theoretical

260 results of the 60° series, which have the lowest energy (Supplementary **Fig. 20**), are included in this

261 discussion, while the other two series are presented in Supplementary **Figs. 22-23**. Second, the

262 evolution of the energy profile after applying an electric field in the z-direction was explored (**Fig.**

263 **4b**, top). From the energy profile observed under rotations, two local minima, namely 0° and 80°

264 were identified (0° and 160° represent the same structure).

265 The dipole moment in the transport direction (z) is of primary interest since this moment is the

266 direction of the experimentally applied electric field (**Fig. 4b**, bottom). The z-components of the

267 dipole moment at 0° and 80° are approximately -1 Debye and 2 Debye, respectively. With their

268 different signs, they respond to the electric field in opposite ways. When a positive electric field is

269 applied, the cluster prefers to adopt the orientation of State I, while the energy of State II decreases

270 under a negative electric field (Supplementary **Fig. 21**). The energy barrier is estimated by selecting

271 the orientation with a zero dipole in the z-direction. Then, the energy barrier evolution under an

272 electric field increasing in the -z-direction is studied (**Fig. 4c**). As expected, the energy barrier

273 decreases with increasing electric field.[5,7] When the electric field reaches 1.2 V/Å, the energy barrier

274 becomes negligible, and State II has the lowest energy, indicating that State I can be switched to

275 State II under a negative threshold electric field.

276 Finally, the two structures corresponding to States I and II were embedded within two gold

277 electrodes (**Figs. 2c-2d**). The Au-Au distance of the theoretical models is ~1.2 nm, which is

278 consistent with the experimental results (~1.15 nm). Based on the junction models, the DFT-based

279 mean-field Hamiltonians were extracted and used to calculate the electrical conductance using the

280 transport code GOLLUM.[56] As shown in Fig. 4d, where the corresponding transmission functions

281 are plotted as blue and red curves, respectively, the conductance of one state differs from the other

282 over almost the whole energy range between the HOMO and LUMO, leading to a possible switching

283 ratio from ~250% to ~1000% according to $R = \frac{\log T_{\text{State I}}}{\log T_{\text{State II}}} \times 100\%$, which is consistent with the

284 experimentally measured conductance of the two states. In the other two series discussed in

285 Supplementary **Figs. 22-23**, e.g. 80° or 130°, similar local minimum and electric-field-dependent

286 energy barrier evolutions are also predicted, indicating that the two-state memristive behavior

287 results from dipole reorientation within the junctions. The actual energy barrier in the experiment

288 could be higher than those calculated because our preliminary theoretical calculations represent a

289 lower bound, since full relaxation is carried out at each rotation step. To demonstrate this point, we

290 also calculated energy barriers without relaxation at each rotation step. This clearly demonstrates

291 that the energy barrier increases if the fullerene cage is not fully relaxed (Supplementary **Fig. 23a**).

292 The results in Supplementary Fig. 18 therefore suggest a trend, but the absolute energy barriers

293 could very probably be higher than calculated. The energy profiles of [Sc_2C_2] cluster rotations in

Sc$_2$C$_2$@D_{2d}(23)-C$_{84}$ and Sc$_2$C$_2$@C_{2v}(9)-C$_{86}$ were calculated ==in the same way. As demonstrated in==

==Supplementary **Fig. 24b-24c**, the actual energy barrier of Sc$_2$C$_2$@C_{2v}(9)-C$_{86}$ is between 0.5 and 2.5==

==eV, whereas Sc$_2$C$_2$@D_{2d}(23)-C$_{84}$ has a much higher barrier, ranging from 1.0 eV to 4.7 eV, which==

==is higher than that of Sc$_2$C$_2$@Cs(hept)-C$_{88}$ (~0.2 to ~1.7 eV),== suggesting that Sc$_2$C$_2$@Cs(hept)-C$_{88}$

is a good candidate with a low operating voltage.

Conclusions

In this work, logic-in-memory operations of a two-terminal single-metallofullerene device at room

temperature were demonstrated. The digital information was found to be reversibly encoded and

stored by manipulating the movement of the independent permanent dipole of [Sc$_2$C$_2$] in the

fullerene cage using a pulsed bias voltage. Since the [Sc$_2$C$_2$] group is encapsulated in the cage, the

inter-dipole coupling between adjacent devices is expected to be lower than the energy barrier U;

hence, these devices have the potential for high-density integration. The demonstration of fourteen

basic Boolean logic functions at the single-molecule level using sequential operational cycles offers

new insights into the development of future in-memory and neuromorphic computing. Due to the

technological challenges in microfabrication processes, compared to a gate-controlled three-

terminal device, our two-terminal device has significant advantages for future integration.

Furthermore, our work suggests that metallofullerenes and more generally, supramolecular cages

with an encapsulated single dipole group, are a plausible direction to design target molecules for

single-molecule logic-in-memory devices.

Methods

316 **Preparation of molecules**. A powder containing metallofullerene $Sc_2C_2@D_{2d}(23)$-C_{84},

317 $Sc_2C_2@C_{2v}(9)$-C_{86} and $Sc_2C_2@C_s$(hept)-C88 (Supplementary **Fig. 26**) was synthesized in an arc-

318 discharge reactor (FAF-1/2, Shenyang Keyou Vacuum Technology Co., Ltd., China) by the

319 optimized Krätschmer-Huffman arc-discharge method.[37,57] Briefly, a graphite rod packed with

320 Sc_2O_3/graphite powder with a weight ratio of 0.38/1 was installed as the anode in the arc reactor.

321 This reactor was vacuumed, and then, 200 Torr He was introduced as the arcing reaction atmosphere.

322 The packed graphite rod was preheated with a 175 A direct current for 30 min in close contact with

323 a graphite cathode and then moved back to generate an arcing area between the anode and cathode

324 under a 100 A direct current. Fullerene-containing soot generated in this arcing area was collected

325 when the arcing reaction was finished. Such an arcing synthesis process was repeated more than

326 100 times to accumulate sufficient samples of fullerene. The produced powder was extracted in

327 toluene using a supersonic cleaner for 1 h, and this extraction process was repeated three times. The

328 isolation of the targeted endohedral fullerenes was performed on an LC-6AD HPLC instrument

329 (Shimadzu Corporation, Japan) with UV detection at 330 nm. Five types of COSMISIL columns

330 (Nacalai Tesque Co., Ltd., Japan) were used in the HPLC process, namely, a preparative Buckyprep

331 column (20 × 250 mm), a semi-preparative Buckyprep column (10 × 250 mm), a semi-preparative

332 Buckyprep-M column (10 × 250 mm), a semi-preparative 5PBB column (10 × 250 mm), and two

333 semi-preparative 5NPE columns (10 × 250 mm). Mass spectra were measured on an HCT mass

334 spectrometer (Bruker, USA) using an atmospheric pressure chemical ionization (APCI) source. Vis-

335 NIR absorption spectra were obtained on a Cary 5000 spectrometer (Agilent Technologies, USA).

336

337 **Conductance measurements.** The single-molecule conductance was measured using the scanning

tunneling microscope break-junction (STM-BJ) technique with the home-built setup described previously.[40,41] Unless otherwise stated, all charge transport experiments were performed under atmospheric conditions at room temperature. A gold substrate was fabricated by depositing a 10/200 nm layer of Cr/Au onto a silicon wafer with silicon dioxide. The gold substrate was cleaned with piranha solution before the experiment. A gold tip was created by flame cleaning and annealing to form a gold bead. We drove the gold tip circularly in and out of contact with the gold substrate and continuously recorded the current signal with +0.1 V bias voltage. During the breaking of the gold-gold contact, a molecule may bridge the two electrodes *in-situ*, leading to a conductance plateau. A sampling rate of 20 kHz was used to collect more than 2000 conductance-distance traces to construct the conductance histograms.

Conductance–voltage measurements. The G-V characterization was adopted from a previously modified protocol using the hovering mode of the STM-BJ technique.[45,58] During the break junction process with a +0.1 V bias voltage applied, we observed conductance plateaus formed between 10^{-2} and 10^{-3} G_0 for $Sc_2C_2@C_s$(hept)-C_{88} . We then stopped the movement of the gold tip and scanned the bias voltage with a cyclic sequence from 0 V → 1 V→ 0 V → -1 V→ 0 V (**Figs. 2c-2d**). Before and after the voltage scan, we set the bias to +0.2 V and checked whether the measured conductance was still in the same conductance range. The G-V traces in which the conductance remained in the same conductance range before and after the voltage scan were selected for analysis.

Two types of G-V traces with open hysteresis loops or non-open loops were observed (Supplementary Fig. 1). The hysteresis loop was determined by the gap within the loop, *i.e.*, the gap between the forward scanning curve and the reverse scanning curve. For a forward scanning curve

360 *f* and the corresponding reverse scanning curve *r*, both n-point *G-V* curves, the gap *d* is calculated

361 as

362 $$d_{xy} = \sum_{i=1}^{n}(f_i - r_i)^2 \quad (2)$$

363 If $d_{xy} < d_t$, the corresponding loop is regarded as a non-hysteresis loop (Supplementary **Fig. 1b**);

364 otherwise, it is regarded as a hysteresis loop, where d_t is a threshold value that was determined by

365 observing the overlapping of the forward and the reverse curve. For molecules with a polarized

366 permanent dipole, the single-molecule junction has two types of geometries: those with a polarized

367 dipole pointing towards the tip, and those pointing away from the tip (left column of **Figs. 2c-2d**).

368 The curves with open hysteresis loops are divided into two sets, according to the conductance value

369 at -0.3 V in the two scan processes of -1 V → 0 V and 0 V → -1 V, and then overlaid on a

370 logarithmic scale to display a two-dimensional *G–V* histogram (Supplementary **Figs. 3-4**). The

371 statistically most likely conductance levels were determined by creating conductance histograms at

372 arbitrary voltages. This approach provides distinct accumulated peaks.[59] Based on these peaks,

373 individual *G–V* curves can be identified within the initial datasets that represent the statistically

374 most probable transport characteristics. We used a 200*200 matrix to plot the 2D *G-V* histograms.

375 The matrix was achieved by evenly spacing the conductance (in a logarithmic scale) and voltage (in

376 a linear scale). Each *G-V* trace is analyzed in this matrix, which is combined with all the matrices

377 of the *G-V* traces to obtain the matrix of the 2D conductance histogram. The data density is presented

378 in different colors according to the color bar. We used the Gaussian function to fit each column of

379 the 2D conductance histogram to obtain the Gaussian peaks and thus obtained the fitting line.

380

381 **The *in-situ* bias voltage controlled switching and logic operation.** The *in-situ* experiments were

382   also based on the hovering mode of the STM-BJ technique.[45,58] First, we measured the bias voltage

383   controlled switching and non-volatile memory behavior. Since the statistical threshold voltage is

384   ~±0.7 V, we selected ±0.8 V as the switching voltage. To observe a conductance more obviously

385   different between the bistable states, we chose +0.2 V to read out the conductance of the molecular

386   states. To ensure data collection, we treated +0.01 V as 0 bias voltage during the measurements. It

387   should be noted that the conductance value of the molecule at +0.01 V is not accurate because the

388   signal-to-noise ratio is very low under this low bias voltage in our equipment. To further analyze

389   the stability and reproducibility of the single-fullerene junction, the typical lifetime of the molecular

390   junctions with different voltage pulses are counted (Supplementary **Figs. 6-10, 14**) and discussed in

391   Supplementary Information S3 and S4.

392   After the non-volatile memory behavior was confirmed, we realized the fundamental logic

393   operations for in-memory computing. The logic operations are based on Boolean functions. We

394   designed pulsed bias voltage sequences to realize the fourteen logic operations, namely, TRUE,

395   FALSE, IMP, RIMP, NIMP, RNIMP, p, q, not p, not q, OR, NAND, NOR and AND.

396

397   **Theoretical calculations.** Geometrical optimization was performed using the DFT code SIESTA[49],

398   with a local density approximate LDA functional, a double-ζ polarized basis, cut-off energy of 200

399   Ry, and a 0.04 eV/Å force tolerance. To compute their electrical conductance, the molecules were

400   each placed between two Au electrodes. For each structure, the transmission coefficient $T(E)$

401   describing the propagation of electrons of energy E from the left to the right electrode was calculated

402   using GOLLUM code[56], which combines the mean-field Hamiltonian and overlap matrices of the

403   DFT code SIESTA with Landauer-based quantum transport theory using the expression

404 $$T(E) = Tr\left[\Gamma_{\mathrm{L}}(E)G_{\mathrm{r}}(E)\Gamma_{\mathrm{R}}(E)G_{\mathrm{r}}^{\dagger}(E)\right] \quad (3)$$

405 where $\Gamma_{\mathrm{L,R}}(E) = i\left(\sum_{\mathrm{L,R}}(E) - \sum_{\mathrm{L,R}}^{\dagger}(E)\right)/2$, $G_{r}(E) = \left(g^{-1} - \Sigma_{\mathrm{L}} - \Sigma_{\mathrm{R}}\right)^{-1}$, g is Green's function of the

406 isolated molecule, $\Gamma_{\mathrm{L,R}}$ determines the widths of transmission resonances, $\sum_{\mathrm{L,R}}(E)$ are the self-

407 energies describing the contact between the molecule and left (L) and right (R) electrodes and G_{r} is

408 the retarded Green's function of the molecule in the presence of the electrodes. The low-temperature

409 conductance is extracted from the transmission spectrum and evaluated by the following formula:

410 $G = G_0 T(E_{\mathrm{F}})$, where $G_0 = 2e^2/h$ is the conductance quantum, h is Planck's constant, e is the charge of

411 a proton and E_{F} is the Fermi energy.

412 To calculate the binding energy using SIESTA, we used a counterpoise method to correct for basis

413 set superposition errors that are inherent with the localized orbital basis sets that are employed. The

414 binding energy between the $Sc_2C_2@C_s$(hept)-C_{88} and the gold tip is shown in Supplementary Fig.

415 17b. The molecule $Sc_2C_2@C_s$(hept)-C_{88} is defined as entity A and the gold tip is defined as entity

416 B. The ground state energy of the total system was calculated using SIESTA and is denoted as E_{AB}^{AB}

417 with the DFT parameters defined previously. The energy of each entity was then calculated on a

418 fixed basis, using ghost atoms. Hence, the energy of the molecule in the presence of the fixed basis

419 is defined as E_A^{AB} and for gold as E_B^{AB}. The binding energy (BE) was then calculated using the

420 following equation: BE = $E_{AB}^{AB} - E_A^{AB} - E_B^{AB}$. The binding energy was calculated as a function of the

421 rotation angle.

422 Transition states (TS) calculations were carried out using a damped molecular dynamics algorithm

423 combined with the climbing-image nudged elastic band (CI-NEB) method[54,55] within Vienna Ab

424 initio Simulation Package (VASP 5.4.4).[52,53] The projector augmented wave (PAW)

425 pseudopotentials[60] and the Perdew–Burke–Ernzerhof (PBE) scheme[61] for the exchange and

correlation energy are employed in calculation. The energy cut-off is set to 400 eV. An 30×30×30 Å^3 supercell is used to model isolated $Sc_2C_2@Cs$(hept)-C_{88}. The Γ-point was used to sample the first Brillouin zone. During the CI-NEB calculation, the structural optimization would be completed when the maximum forces on all atoms were smaller than 0.05 eV/Å. Three TSs were revealed in the 0º to 20º, 20º to 50º, and 50º to 70º zones, respectively (Supplementary Fig. 18b).

Data availability

All the data supporting the plots within this paper and the findings of this study are available from the corresponding author upon request.

Code availability

The data analysis was accomplished in our open-source code XME analysis (https://github.com/Pilab-XMU/XMe_DataAnalysis).

References

1   LeCun, Y., Bengio, Y. & Hinton, G. Deep learning. *Nature* **521**, 436-444 (2015).
2   Mead, C. Neuromorphic electronic systems. *Proc. IEEE* **78**, 1629-1636 (1990).
3   Furber, S. To build a brain. *IEEE Spectr.* **49**, 44-49 (2012).
4   Khajetoorians, A. A., Wiebe, J., Chilian, B. & Wiesendanger, R. Realizing all-spin-based logic operations atom by atom. *Science* **332**, 1062-1064 (2011).
5   Zhang, K. *et al.* A Gd@C82 single-molecule electret. *Nat. Nanotechol.* **15**, 1019–1024 (2020).
6   Yang, Q. *et al.* Design of Single-Molecule Multiferroics for Efficient Ultrahigh-Density Nonvolatile Memories. *Adv. Sci.* **6**, 1801572 (2019).
7   Jaroš, A., Bonab, E. F., Straka, M. & Foroutan-Nejad, C. Fullerene-Based Switching Molecular Diodes Controlled by Oriented External Electric Fields. *J. Am. Chem. Soc.* **141**, 19644-19654 (2019).
8   Linn, E., Rosezin, R., Tappertzhofen, S., Bottger, U. & Waser, R. Beyond von Neumann--logic operations in passive crossbar arrays alongside memory operations. *Nanotechnology* **23**, 305205 (2012).
9   Borghetti, J. *et al.* 'Memristive' switches enable 'stateful' logic operations via material implication. *Nature* **464**, 873-876 (2010).

456   10   Yang, J. J., Strukov, D. B. & Stewart, D. R. Memristive devices for computing. *Nat. Nanotechol.*
457   **8**, 13-24 (2013).

458   11   Strukov, D. B., Snider, G. S., Stewart, D. R. & Williams, R. S. The missing memristor found.
459   *Nature* **453**, 80-83 (2008).

460   12   Ielmini, D. & Wong, H. S. P. In-memory computing with resistive switching devices. *Nat.*
461   *Electron.* **1**, 333-343 (2018).

462   13   Zhang, W., Mazzarello, R., Wuttig, M. & Ma, E. Designing crystallization in phase-change
463   materials for universal memory and neuro-inspired computing. *Nat. Rev. Mater.* **4**, 150-168,
464   (2019).

465   14   Grollier, J. *et al.* Neuromorphic Spintronics. *Nat. Electron.* **3**, 360–370 (2020).

466   15   Guo, R., Lin, W., Yan, X., Venkatesan, T. & Chen, J. Ferroic tunnel junctions and their
467   application in neuromorphic networks. *Appl. Phys. Rev.* **7**, 011304 (2020).

468   16   Wang, P. & Yu, S. Ferroelectric devices and circuits for neuro-inspired computing. *MRS*
469   *Commun.* **10**, 538-548 (2020).

470   17   Cho, B. *et al.* Rewritable switching of one diode-one resistor nonvolatile organic memory
471   devices. *Adv. Mater.* **22**, 1228-1232 (2010).

472   18   Han, S.-T., Zhou, Y. & Roy, V. A. L. Towards the Development of Flexible Non-Volatile
473   Memories. *Adv. Mater.* **25**, 5425-5449 (2013).

474   19   Cho, B., Song, S., Ji, Y., Kim, T.-W. & Lee, T. Organic Resistive Memory Devices: Performance
475   Enhancement, Integration, and Advanced Architectures. *Adv. Funct. Mater.* **21**, 2806-2829
476   (2011).

477   20   Goswami, S. *et al.* Charge disproportionate molecular redox for discrete memristive and
478   memcapacitive switching. *Nat. Nanotechnol.* **15**, 380–389 (2020).

479   21   Goswami, S. *et al.* Robust resistive memory devices using solution-processable metal-
480   coordinated azo aromatics. *Nat. Mater.* **16**, 1216-1224 (2017).

481   22   Han, Y. *et al.* Electric-field-driven dual-functional molecular switches in tunnel junctions. *Nat.*
482   *Mater.* **19**, 843-848 (2020).

483   23   Busche, C. *et al.* Design and fabrication of memory devices based on nanoscale
484   polyoxometalate clusters. *Nature* **515**, 545-549 (2014).

485   24   Goswami, S. *et al.* Decision trees within a molecular memristor. *Nature* **597**, 51-56 (2021).

486   25   Lörtscher, E., Ciszek, J. W., Tour, J. & Riel, H. J. S. Reversible and controllable switching of a
487   single-molecule junction. *Small* **2**, 973-977 (2006).

488   26   Li, H. B., Tebikachew, B. E., Wiberg, C., Moth-Poulsen, K. & Hihath, J. A Memristive Element
489   Based on an Electrically Controlled Single-Molecule Reaction. *Angew. Chem. Int. Ed.* **59**,
490   11641-11646 (2020).

491   27   Nishihara, S. *Nat. Nanotechol.* **15**, 966-967 (2020).

492   28   Kato, C. *et al.* Giant Hysteretic Single-Molecule Electric Polarisation Switching above Room
493   Temperature. *Angew. Chem. Int. Ed.* **57**, 13429-13432 (2018).

494   29   Sessoli, R. *et al.* High-spin molecules: [$Mn_{12}O_{12}(O_2CR)_{16}(H_2O)_4$]. *J. Am. Chem. Soc.* **115**, 1804-
495   1816 (1993).

496   30   Sessoli, R., Gatteschi, D., Caneschi, A. & Novak, M. A. Magnetic bistability in a metal-ion
497   cluster. *Nature* **365**, 141-143 (1993).

498   31   Meded, V., Bagrets, A., Arnold, A. & Evers, F. J. S. Molecular switch controlled by pulsed bias
499   voltages. *Small* **5**, 2218-2223 (2009).

500 32 Zabala-Lekuona, A., Seco, J. M. & Colacio, E. Single-Molecule Magnets: From Mn12-ac to
501   dysprosium metallocenes, a travel in time. *Coord. Chem. Rev.* **441**, 213984 (2021).
502 33 Ward, D. R., Corley, D. A., Tour, J. M. & Natelson, D. Vibrational and electronic heating in
503   nanoscale junctions. *Nat. Nanotechol.* **6**, 33-38 (2011).
504 34 Twamley, J., Utami, D. W., Goan, H. S. & Milburn, G. Spin-detection in a quantum
505   electromechanical shuttle system. *New J. Phys.* **8**, 63-63 (2006).
506 35 Kurihara, H. *et al.* Sc2C2@C80 rather than Sc2@C82: templated formation of unexpected
507   C2v(5)-C80 and temperature-dependent dynamic motion of internal Sc2C2 cluster. *J. Am. Chem.*
508   *Soc.* **133**, 2382-2385 (2011).
509 36 Foroutan-Nejad, C., Andrushchenko, V. & Straka, M. Dipolar molecules inside C70: an electric
510   field-driven room-temperature single-molecule switch. *Phys. Chem. Chem. Phys.* **18**, 32673-
511   32677 (2016).
512 37 Chen, C. H. *et al.* Zigzag Sc2C2 Carbide Cluster inside a [88]Fullerene Cage with One Heptagon,
513   Sc2C2@Cs(hept)-C88: A Kinetically Trapped Fullerene Formed by C2 Insertion? *J. Am. Chem.*
514   *Soc.* **138**, 13030-13037 (2016).
515 38 Deng, Q. & Popov, A. A. Clusters encapsulated in endohedral metallofullerenes: how strained
516   are they? *J. Am. Chem. Soc.* **136**, 4257-4264 (2014).
517 39 Jin, P., Tang, C. & Chen, Z. Carbon atoms trapped in cages: Metal carbide clusterfullerenes.
518   *Coord. Chem. Rev.* **270-271**, 89-111 (2014).
519 40 Venkataraman, L., Klare, J. E., Nuckolls, C., Hybertsen, M. S. & Steigerwald, M. L.
520   Dependence of single-molecule junction conductance on molecular conformation. *Nature* **442**,
521   904-907 (2006).
522 41 Xu, B. & Tao, N. J. Measurement of single-molecule resistance by repeated formation of
523   molecular junctions. *Science* **301**, 1221-1223 (2003).
524 42 Hong, W. *et al.* Single molecular conductance of tolanes: experimental and theoretical study on
525   the junction evolution dependent on the anchoring group. *J. Am. Chem. Soc.* **134**, 2292-2304
526   (2012).
527 43 Moreno-Garcia, P. *et al.* Charge transport in C60-based dumbbell-type molecules: mechanically
528   induced switching between two distinct conductance states. *J. Am. Chem. Soc.* **137**, 2318-2327
529   (2015).
530 44 Rincon-Garcia, L. *et al.* Molecular design and control of fullerene-based bi-thermoelectric
531   materials. *Nat. Mater.* **15**, 289-293 (2016).
532 45 Bai, J. *et al.* Anti-resonance features of destructive quantum interference in single-molecule
533   thiophene junctions achieved by electrochemical gating. *Nat. Mater.* **18**, 364-369 (2019).
534 46 Chandler, H. J., Stefanou, M., Campbell, E. E. B. & Schaub, R. Li@C60 as a multi-state
535   molecular switch. *Nat. Commun.* **10**, 2283 (2019).
536 47 Huang, T. *et al.* A molecular switch based on current-driven rotation of an encapsulated cluster
537   within a fullerene cage. *Nano Lett.* **11**, 5327-5332 (2011).
538 48 Miyamachi, T. *et al.* Robust spin crossover and memristance across a single molecule. *Nat.*
539   *Commun.* **3**, 938 (2012).
540 49 Soler, J. M. *et al.* The SIESTA method forab initioorder-Nmaterials simulation. *J. Phys.:*
541   *Condens. Matter.* **14**, 2745-2779 (2002).
542 50 Morley, G. W. *et al.* Hyperfine structure of Sc@C82 from ESR and DFT. *Nanotechnology* **16**,
543   2469-2473 (2005).

544 51 Leigh, D. F. *et al.* Distinguishing two isomers of Nd@C$_{82}$ by scanning tunneling microscopy
545   and density functional theory. *Chem. Phys. Lett.* **414**, 307-310 (2005).
546 52 Kresse, G. & Furthmüller, J. Efficiency of ab-initio total energy calculations for metals and
547   semiconductors using a plane-wave basis set. *Comput. Mater. Sci.* **6**, 15-50 (1996).
548 53 Kresse, G. & Furthmüller, J. Efficient iterative schemes for ab initio total-energy calculations
549   using a plane-wave basis set. *Phys. Rev. B* **54**, 11169-11186 (1996).
550 54 Henkelman, G. & Jónsson, H. Improved tangent estimate in the nudged elastic band method for
551   finding minimum energy paths and saddle points. *J. Chem. Phys.* **113**, 9978-9985 (2000).
552 55 Henkelman, G., Uberuaga, B. P. & Jónsson, H. A climbing image nudged elastic band method
553   for finding saddle points and minimum energy paths. *J. Chem. Phys.* **113**, 9901-9904 (2000).
554 56 Ferrer, J. *et al.* GOLLUM: a next-generation simulation tool for electron, thermal and spin
555   transport. *New J. Phys.* **16**, 093029 (2014).
556 57 Yao, Y.-R. *et al.* Atomically Precise Insights into Metal–Metal Bonds Using Comparable Endo-
557   Units of Sc$_2$ and Sc$_2$C$_2$. *CCS Chem.* **3**, 294-302 (2021).
558 58 Capozzi, B. *et al.* Single-molecule diodes with high rectification ratios through environmental
559   control. *Nat. Nanotechol.* **10**, 522-527 (2015).
560 59 Schwarz, F. *et al.* Charge Transport and Conductance Switching of Redox-Active Azulene
561   Derivatives. *Angew. Chem. Int. Ed.* **55**, 11781-11786 (2016).
562 60 Blöchl, P. E. Projector augmented-wave method. *Phys. Rev. B* **50**, 17953-17979 (1994).
563 61 Perdew, J. P., Burke, K. & Ernzerhof, M. Generalized Gradient Approximation Made Simple.
564   *Phys. Rev. Lett.* **77**, 3865-3868 (1996).

565

572 **Author contributions** W.H., S.X., and J.L. conceived the idea for the paper. Y.Yao and S.X.

573 synthesized and characterized the endohedral metallofullerenes molecule. J.Z. fabricated the MCBJ

574 chips. J.L., H.C.W., X.L., J.S., C.Z., and J.Z. measured the conductance, conductance-voltage and

575 characterization of the *in-situ* logic operation. S.H., Q.W., and C.L. conducted the theoretic

576 calculations. J.L., H.Z., Y.W., and C.Z. discussed and produced the picture. C.T., M.W., J.Y.L.,

577 W.X., and, Y.Yang help to discuss the mechanism. Z.P. and L.K. supports the data analysis. J.L.,

578 S.H., Q.W., C. L., S.X., and W. H. analyzed and discussed the data and wrote the paper.

579 **Competing interests** The authors declare no competing interests